Highlights

Numerical analysis of the twin tunnels with transverse galleries using plastic and viscous constitutive models for rockmass and lining

Quevedo, F. P. M.,Colombo, C. A. M. M.,Bernaud, D.,Maghous, S.

- Qualquer coisa 1
- Qualquer coisa 2
- Qualquer coisa 3

Numerical analysis of the twin tunnels with transverse galleries using plastic and viscous constitutive models for rockmass and lining

Quevedo, F. P. M.[a,*], Colombo, C. A. M. M.[a], Bernaud, D.[a] and Maghous, S.[a]

[a] *Federal University of Rio Grande do Sul, Av. Osvaldo Aranha, 99, Porto Alegre, 90.035-190, RS, Brazil*

ARTICLE INFO

Keywords:
twin tunnels
transverse gallery
constitutive models
finite element method

ABSTRACT

This paper aims to demonstrate the long-term implications of the rheological constitutive behavior of rock mass and concrete lining in the convergence of the intersection area of twin tunnel galleries using a three-dimensional numerical analysis based on the finite-element method. A Drucker-Prager-Perzyna elastoplastic-viscoplastic constitutive law represents the rock mass and, for the lining, an elastic and viscoelastic law. The deactivation-activation methods simulate the excavation process. Comparisons of convergence reveal that the viscous effects of the rock mass and the lining significantly influence the peak convergence within the intersection zone, resulting in differences of approximately 10% in convergence values.

1. Introduction

The structural design of deep twin tunnels involves estimating cross-section convergence, lining pressure, and the size of the plastic zone within the rock mass caused by the excavation process. The final convergence and stress field around the tunnel depend on *in situ* initial stresses, cross-section geometry, and the coupling between the lining and the rock mass during construction. Unlinke a single tunnel, the proximity between twin tunnels break the symmetry of deformations in tunnel wall. Many twin tunnels have transverse galleries that serve as emergency routes. These galleries will introduce a local effect on the convergence profile of the longitudinal tunnel.

Additionaly, the rheological behavior of the rockmass and lining plays a crucial role in how stress and displacements fields evolve over time.

Indicar os objectivos do trabalho e fornecer um contexto adequado, evitando uma pesquisa bibliográfica ou um resumo dos resultados.

2. Statement of problem and fundamental assumptions

3. Constitutive Model of the Rock Material

An elastoplastic-viscoplastic constitutive model was implemented in ANSYS using the UPF/USERMAT customization tool [1] to simulate rock mass. This model concern a serial association of the plastic and viscoplastic constitutive models, i.e., the total strain $\dot{\boldsymbol{\varepsilon}} = \dot{\boldsymbol{\varepsilon}}^e + \dot{\boldsymbol{\varepsilon}}^p + \dot{\boldsymbol{\varepsilon}}^{vp}$, which leads to the following linear constitutive relationship:

$$\dot{\boldsymbol{\sigma}} = \boldsymbol{D} : \dot{\boldsymbol{\varepsilon}}^e = \boldsymbol{D} : (\dot{\boldsymbol{\varepsilon}} - \dot{\boldsymbol{\varepsilon}}^p - \dot{\boldsymbol{\varepsilon}}^{vp}), \tag{1}$$

where $\dot{\boldsymbol{\varepsilon}}^e$, $\dot{\boldsymbol{\varepsilon}}^p$ and $\dot{\boldsymbol{\varepsilon}}^{vp}$, represent the elastic, plastic and viscoplastic strain rate, respectively and $\boldsymbol{D}$ denote the fourth-order isotropic elastic linear constitutive tensor. The one-dimensional representation in Fig. 1 shows this association.

*Corresponding author.

motta.quevedo@ufrgs.br (Q.F.P. M.); carlos.colombo@ufrgs.br (C.C.A.M. M.); denise.bernaud@ufrgs.br (B. D.); samir.maghous@ufrgs.br (M. S.)

https://www.researchgate.net/profile/Felipe-Pinto-Da-Motta-Quevedo (Q.F.P. M.); http://lattes.cnpq.br/4919388217690564 (C.C.A.M. M.); http://lattes.cnpq.br/2809615143819128 (B. D.); http://lattes.cnpq.br/6305244914209829 (M. S.)

ORCID(s): 0000-0003-4171-1696 (Q.F.P. M.); 0000-0000-0000-0000 (C.C.A.M. M.); 0000-0001-6365-3269 (B. D.); 0000-0002-1123-3411 (M. S.)

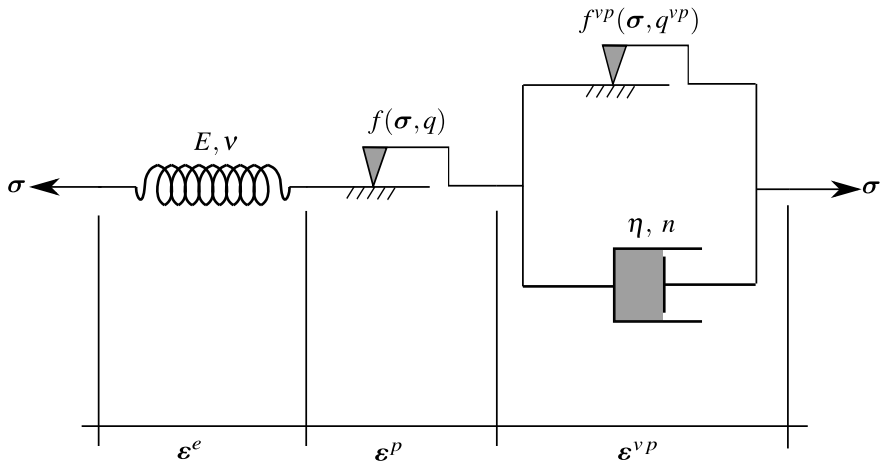

Figure 1: Rheological representation of the elastoplastic-viscoplastic model.

In this model is used a Drucker-Prager plastic flow surface given by

$$f(\boldsymbol{\sigma}, q) = f(I_1, J_2, q) = \beta_1 I_1 + \beta_2 \sqrt{J_2} - q(\alpha), \tag{2}$$

which I_1 is the first invariant of the stress tensor, J_2 the second invariant of the deviator tensor and β_1, β_2 and $q(\alpha)$ are strength parameters related to the friction angle ϕ and cohesion $c(\alpha)$, respectively. In the present model Drucker-Prager surface been inner of the Mohr-Coulomb surface [4], that is,

$$\beta_1 = \frac{(k-1)}{3}, \quad \beta_2 = \frac{(2k+1)}{\sqrt{3}}, \quad q(\alpha) = 2\sqrt{k}\, c(\alpha), \tag{3}$$

where $k = (1 + \sin\phi)/(1 - \sin\phi)$. The internal variable α is the equivalent plastic strain $\bar{\varepsilon}^p$ used to simulate strain hardening/softening phenomena. However, for this study, we adopt perfect plasticity, meaning that c is a constant. For the viscoplasticity surface f^{vp} the same surface is empolyed, but with ϕ^{vp} in β_1 and β_2, and $q^{vp} = 2\sqrt{k^{vp}} - c^{vp}$ where $k^{vp} = (1 + \sin\phi^{vp})/(1 - \sin\phi^{vp})$ and c^{vp} is a constant, i.e., perfect viscoplasticity.

The plastic flow rule is given by:

$$\dot{\boldsymbol{\varepsilon}}^p = \begin{cases} \dot{\lambda}\dfrac{\partial g}{\partial \boldsymbol{\sigma}} & \text{for } f > 0 \\ \mathbf{0}, & \text{for } f \leq 0 \end{cases}, \tag{4}$$

where $\dot{\lambda}$ is the plasticity multiplier and g is a potencial flow analogous to f to simulate the volume dilatation during the evolution of plastic deformations. However, for this analysis, was used associated plasticity, i.e., $g = f$. The plastic multiplier is obtained through the consistency condition $\dot{f} = 0$. Numerical details of this implementation can be found in [9]. For viscoplastic flow rule we have,

$$\dot{\boldsymbol{\varepsilon}}^{vp} = \dot{\lambda}^{vp} \frac{\partial f^{vp}}{\partial \boldsymbol{\sigma}} \tag{5}$$

In contrast to the plastic multiplier, the viscoplastic multiplier λ^{vp} is independent of a consistency condition. As a result, its expression is explicit. For this study, we utilize the Perzyna model as follows:

$$\dot{\lambda}^{vp} = \frac{\Phi(\boldsymbol{\sigma}, q^{vp})}{\eta} \quad \text{and} \quad \Phi = \left\langle \frac{f^{vp}(\boldsymbol{\sigma}, q^{vp})}{f_0} \right\rangle^n, \tag{6}$$

where Φ is the overstress function, η is the dynamic viscosity constant, n is the dimensionless parameter that gives the form of the power law, f_0 a parameter conveniently adopted and $\langle * \rangle$ is the McCauley function which is 0 when $* < 0$, i.e. viscoplastic flow will only occur when the overstress function is positive.

In this coupled model, when $\phi = \phi^{vp}$, cohesion entirely controls the evolution of local mechanical fields. Specifically, when $c \to \infty$ and $c^{vp} \to \infty$, the system achieves a purely elastic solution. The solution becomes purely elastoviscoplastic with $c \to \infty$, while a pure elastoplastic solution emerges with $c^{vp} \to \infty$. In this study's coupled analysis, we have adopted $c^{vp} < c$, allowing the viscoplastic domain to occur without plasticity. However, in the presence of plasticity, viscous effects become inevitable. Fig. 2 illustrates these domains in principal stress space.

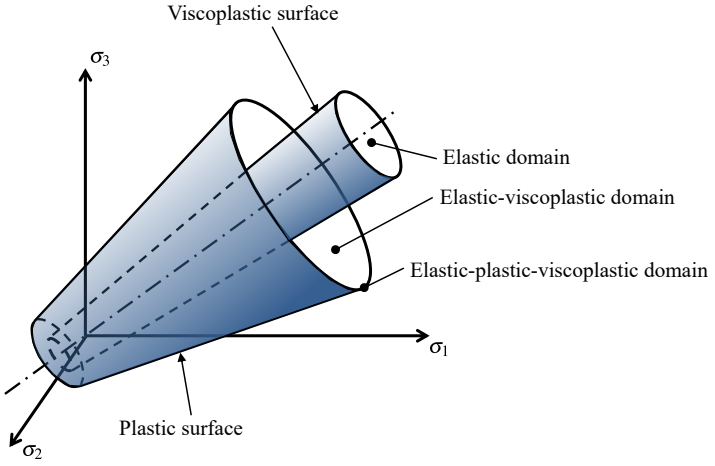

Figure 2: Elastoplastic-viscoplastic domains.

Details of this model, including validations and its application in single tunnel, are in [9]. See [7] for the algorithm details implemented in FORTRAN within the USERMAT subroutine.

4. Constitutive Model of the Lining

We implemented a viscoelastic model in ANSYS using the UPF/USERMAT customization feature [1]. The model simulates concrete creep through a Generalized Kelvin chain, based on Bažant and Prasannan's Solidification Theory [2; 3], with parameter adjustments performed using the CEB-FIP MC90 formulation. The CEB-FIP MC90 formulation also [5] determines the shrinkage component.

In this model, the constitutive relationship between stress and strain is

$$\dot{\boldsymbol{\sigma}} = \boldsymbol{D} : \dot{\boldsymbol{\varepsilon}}^{e} = \boldsymbol{D} : \dot{\boldsymbol{\varepsilon}} - \boldsymbol{D} : \dot{\boldsymbol{\varepsilon}}^{sh} - \boldsymbol{D}^{*} : \dot{\boldsymbol{\varepsilon}}^{cr} \tag{7}$$

where $\dot{\boldsymbol{\varepsilon}}^{sh}$ and $\dot{\boldsymbol{\varepsilon}}^{cr}$ are the shrinkage and creep strain rate, respectively, while $\boldsymbol{D}$ and $\boldsymbol{D}^{*}$ denote the fourth-order isotropic elastic linear constitutive tensor and modified constitutive tensor that incorporates the aging of the concrete, respectively. Due to the time integration scheme for the Newton-Raphson algorithm, the Eq. (7) is given by:

$$\boldsymbol{\sigma}_{n+1} = \boldsymbol{\sigma}_{n} + \boldsymbol{D} : \Delta\boldsymbol{\varepsilon} - \boldsymbol{D} : \Delta\boldsymbol{\varepsilon}^{sh} - \boldsymbol{D}^{*} : \Delta\boldsymbol{\varepsilon}^{cr} \tag{8}$$

in which the increment of shrinkage strain is:

$$\Delta\boldsymbol{\varepsilon}^{sh} = \Delta\varepsilon_{sh}(t_{s})\mathbf{1} \tag{9}$$

where t_{s} represents the concrete curing time, and $\Delta\varepsilon_{sh}$ is the variation of magnitude of the concrete deformation by shrinkage, determined using the expressions of CEB-FIP MC90 [5]. To calculate the increment of creep strain, denoted as $\Delta\boldsymbol{\varepsilon}^{cr}$, we use the incremental algorithm developed by Bažant and Prasannan [2; 3], with an adjustment to incorporate CEB-FIP MC90 formulation. This adaptation is possible comparing the creep functions $\boldsymbol{J}(t, t_{0})$ of both references. This gives to the following equivalence:

$$E_{0} = E_{c}(t_{0}),\ \gamma_{c}(t - t_{0}) = \beta_{c}(t - t_{0}),\ \frac{1}{\upsilon(t)} = \frac{\phi_{0}}{E_{ci}} \text{ and } \frac{1}{\eta(t)} = 0 \tag{10}$$

in which, according to Bažant and Prasannan [2; 3], E_0 is the modulus of elasticity of the concrete aggregates and microscopic particles of the cement paste, $\gamma_c(t - t_0)$ is the microviscoelastic deformation of the volume fraction of solidified concrete $v(t)$, $\eta(t)$ is the apparent macroscopic viscosity and, according to CEB-FIP MC90 [5], $E_c(t_0)$ is the tangent elastic modulus of the concrete at the instant of loading application t_0, $\beta_c(t - t_0)$ is a coefficient that depends on the loading age $t - t_0$, ϕ_0 is a coefficient that depends on the age of the concrete at the instant of loading application and E_{ci} the tangent elasticity modulus of the concrete at the age of 28 day.

Details of this model, including validations and its application in single tunnel, are in [8]. See [6] for the algorithm details implemented in FORTRAN within the USERMAT subroutine.

5. Numerical model

The spatial discretization of the domain corresponds to a mesh with trilinear hexahedral elements (SOLID 185), except in the gallery region, which uses higher-order tetrahedral elements (SOLID186). Fig. 3 shows the mesh, geometric parameters, and boundary conditions for the domain problem. In this figure, d_1 is the distance between longitudinal tunnel axes, R_i longitudinal tunnel cross-section radius, L_2 total excavated length, d_3 domain height, L_1 length of the unexcavated region, L_3 transversal length of the domain, L_p step length of the excavation process, d_2 position of the gallery along the longitudinal tunnel. We considered front, side, and bottom symmetry to reduce computational cost. In conjunction with boundary pressure p, we apply the initial stress condition $\boldsymbol{\sigma}_0 = -p\mathbf{1}$ at all integration points to simulate the initial state of an undisturbed rock mass.

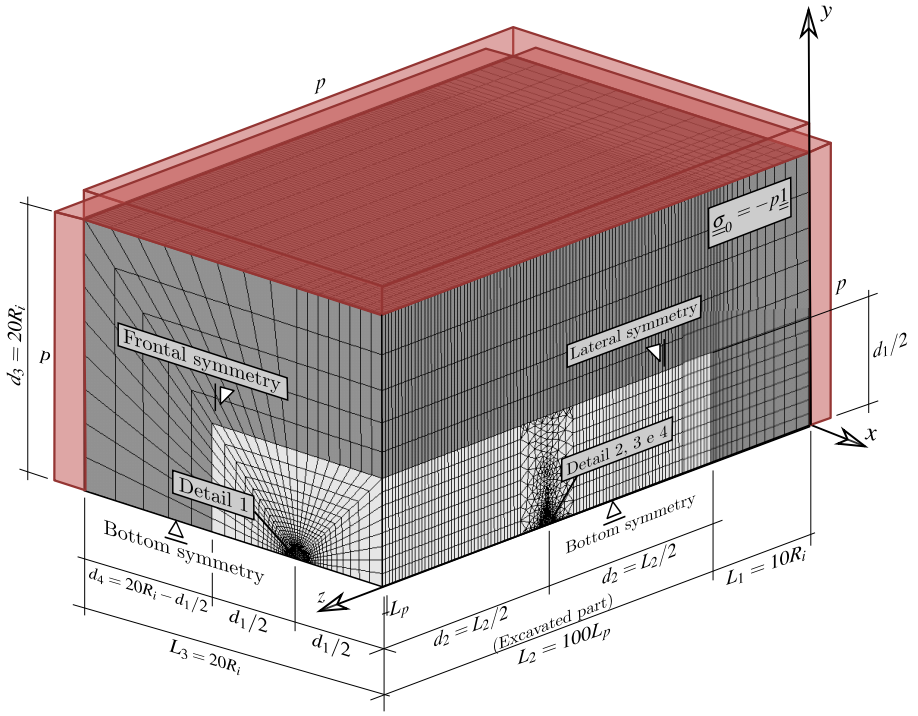

Figure 3: Mesh, dimensions and boundary conditions of the 3D twin tunnel domain

We divided the mesh into two regions: one near the tunnel (light gray), which we refined more, and a region farther away (dark gray). We increased the distortion ratio of elements in the dark gray zone to minimize the number of elements in that region. Due to the low deformation gradient away from the tunnel wall, elements in this area can be considerably larger than in other regions. Fig. 4 shows the mesh at the cross-section of the longitudinal tunnel, with e representing the thickness of the lining.

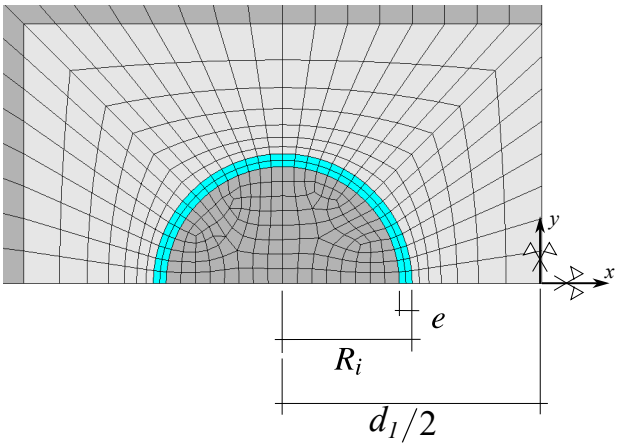

Figure 4: Detail 1 - Mesh in longitudinal tunnel cross-section with spacing $d_1 = 4R_i$

One of the aspects investigated in this work is the influence of the spacing d_1 between longitudinal tunnels of the twin tunnel. Fig. 5 and Fig. 6 illustrate the spatial discretization in the gallery region and its connection with the longitudinal tunnel considering spacings $d_1 = 16R_i, 8R_i$ and $4R_i$, respectively. The dimensions d_5 and d_1 define the size of the transition region comprising tetrahedral elements between the gallery and the rest of the domain. Fig. 7 shows part of this transition region.

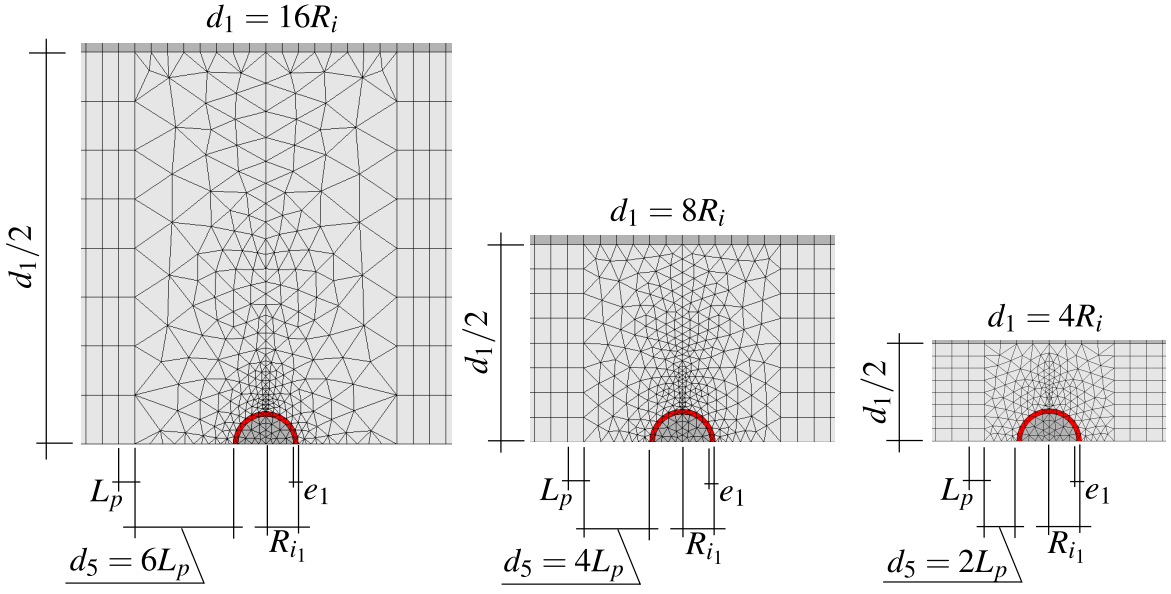

Figure 5: Detail 2 - Side view of the mesh in gallery region with $d_1 = 16R_i$, $d_1 = 8R_i$ and $d_1 = 4R_i$

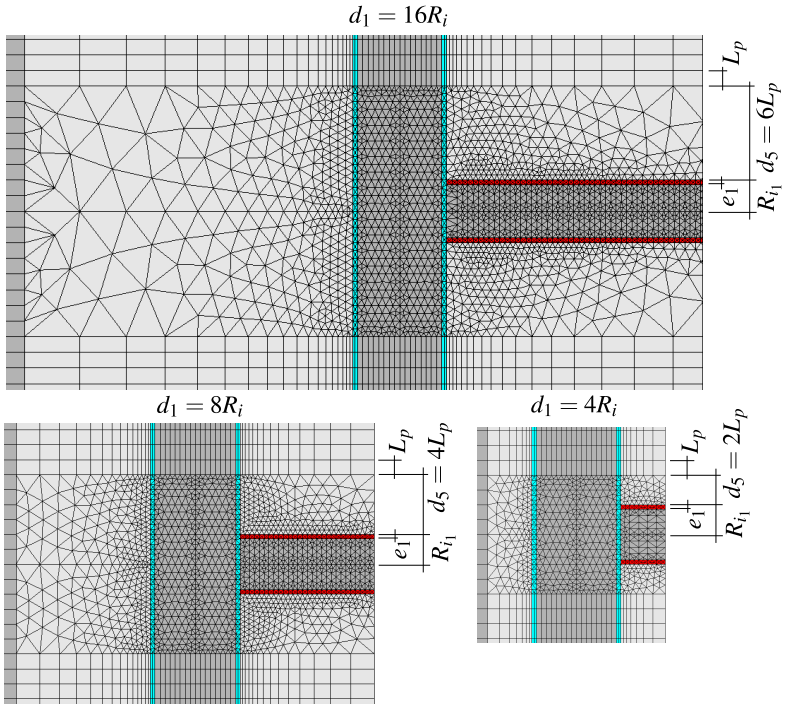

Figure 6: Detail 3 - Bottom view of the mesh in gallery region with $d_1 = 16R_i$, $d_1 = 8R_i$ and $d_1 = 4R_i$

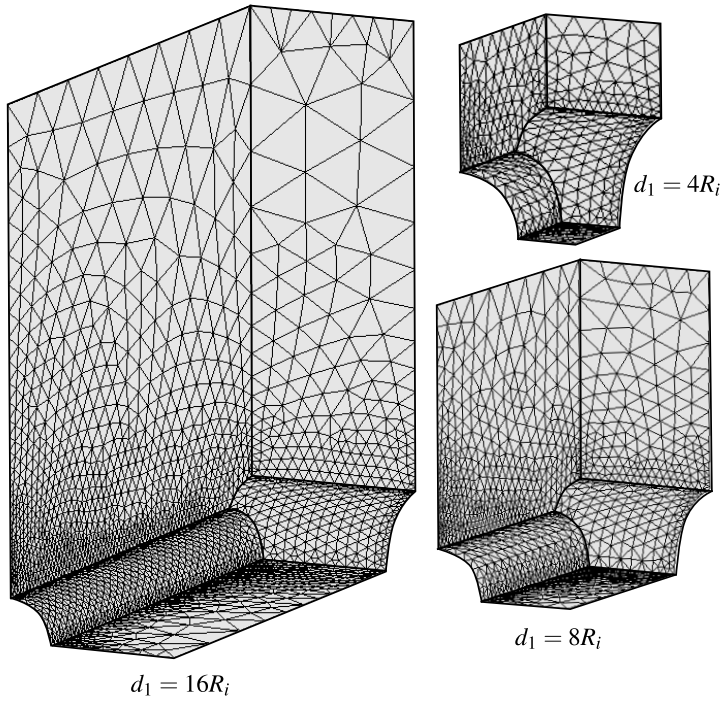

Figure 7: Detail 4 - Isometric view of the portion of the mesh in gallery region $d_1 = 16R_i$, $d_1 = 8R_i$ and $d_1 = 4R_i$

Fig. 8 illustrates the lining mesh, showing the use of tetrahedral elements both in the gallery and at the junction with the longitudinal tunnel. It is crucial to ensure that the boundaries of these tetrahedral elements remain within the length of the excavation step.

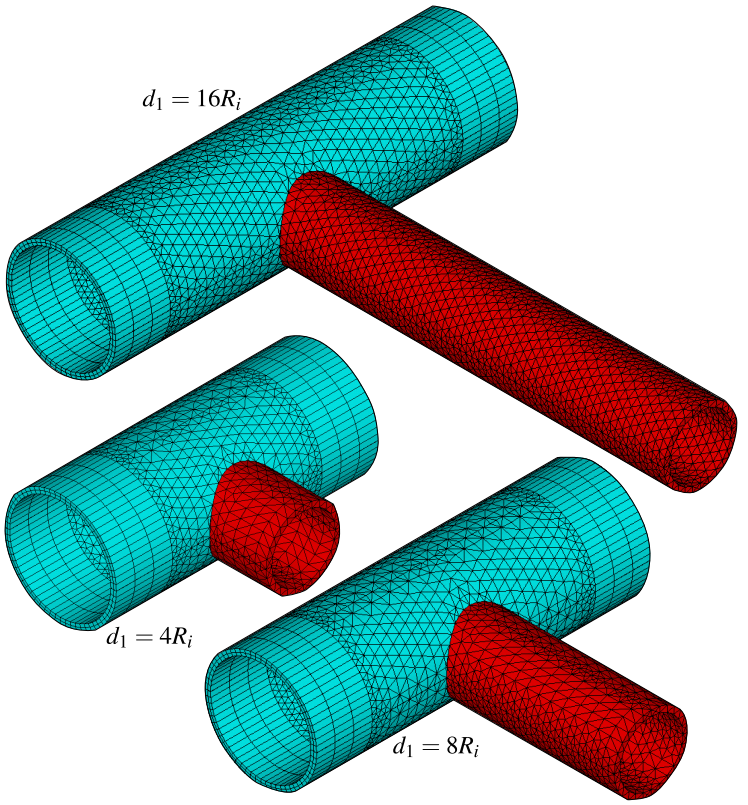

Figure 8: Isometric view of the lining at the intersection for $d_1 = 16R_i$, $d_1 = 8R_i$ and $d_1 = 4R_i$ - expansion of symmetry in the xz plane

The construction process is simulated through the deactivating and activating method, i.e., in each step of excavation, reducing the stiffness of the excavated element (1E-8) and active the lining elements at a distance d_0 from the excavation face (unlined length). With each excavation step, we execute the solution, and time advances based on the expression $t_p = L_p/V_p$, where L_p represents the length of the excavation step, and V_p is the speed of the excavation face. Fig. 9 illustrates a schematic of the excavation process where n_p is the number of excavation steps. In this Figure, n_{pig} represents the number of steps excavated in the longitudinal tunnel that starts gallery excavation. Once reaching this step, we pause the excavation of the longitudinal tunnel, and the gallery excavation begins. In the gallery section, L_{p_1} is the step length of the gallery excavation, V_{p_1} is the speed of the gallery excavation, and d_{0_1} is the unlined length of the gallery. After completing the gallery excavation, the longitudinal tunnel excavation resumes.

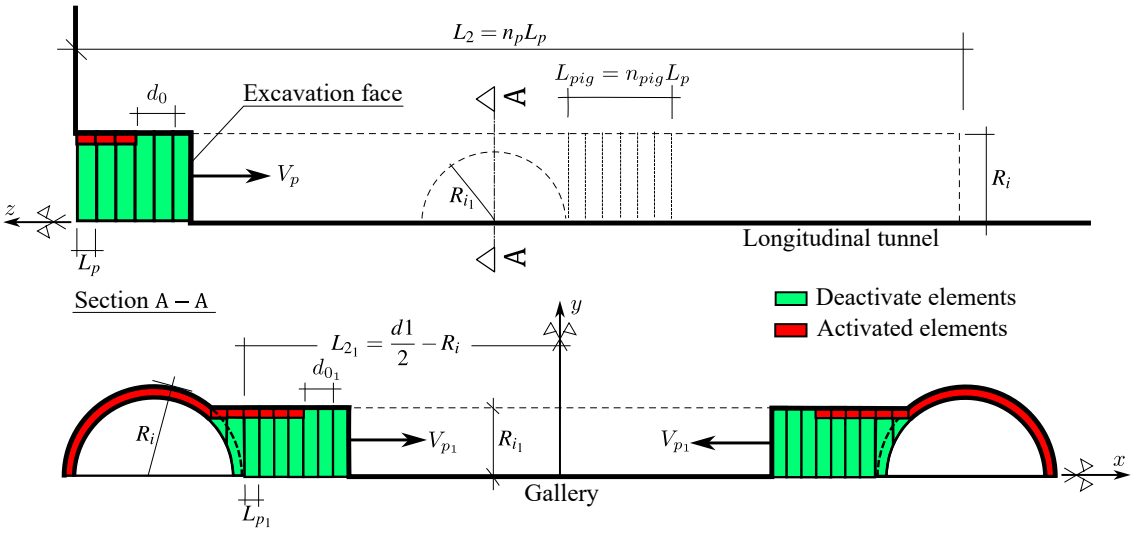

Figure 9: Schematic of the excavation process

6. Comparision with analytical solutions

7. Numerical Results and Discussion

Resultados devem ser claros e concisos

7.1. Influência do afastamento entre os túneis
7.2. A influência da rigidez do revestimento
7.3. A influência da presença da galeria no túnel longitudinal
7.4. Abrangencia da região de influência da galeria
7.5. A influência dos modelos que envolve efeitos diferidos

8. Conclusions

As principais conclusões do estudo podem ser apresentadas numa breve secção de Conclusões, que pode ser autónoma ou constituir uma subsecção de uma secção de Discussão ou de Resultados e Discussão.

9. Appendices

Se houver mais do que um apêndice, estes devem ser identificados como A, B, etc. As fórmulas e equações dos apêndices devem ser numeradas separadamente: Eq. (A.1), Eq. (A.2), etc.; num apêndice seguinte, Eq. (B.1) e assim por diante. O mesmo se aplica aos quadros e figuras: Tabe a A.1; Fig. A.1, etc.

References

ANSYS, 2013. ANSYS Programmer's Reference; release 15.0. Canonsburg, Pennsylvania.

Bažant, Z.P., Prasannan, S., 1989a. Solidification theory for concrete creep. i: Formulation. Journal of engineering mechanics 115, 1691–1703.

Bažant, Z.P., Prasannan, S., 1989b. Solidification theory for concrete creep. ii: Verification and application. Journal of engineering mechanics 115, 1704–1725.

Bernaud, D., 1991. Tunnels profonds dans les milieux viscoplastiques: approches expérimentale et numérique. Ph.D. thesis. Ecole Nationale des Ponts et Chaussées. Paris, French.

CEB-FIP, 1993. CEB-FIP model code 1990: Design code. Comité Euro International du Béton and Fédération Internationale de la Précontrainte (CEB-FIP).

Quevedo, F.P.M., 2017. Comportamento a longo prazo de túneis profundos revestidos com concreto: modelo em elementos finitos. M.S. thesis. Federal University of Rio Grande do Sul. Porto Alegre, Brazil.

Quevedo, F.P.M., 2021. Análise computacional das deformações em túneis profundos considerando o acoplamento plasticidade-viscoplasticidade.

Quevedo, F.P.M., Bernaud, D., Campos Filho, A., 2022a. Numerical analysis of deep tunnels in viscoplastic rock mass considering the creep and shrinkage of the concrete lining. International Journal of Geomechanics 22. doi:10.1061/(ASCE)GM.1943-5622.0002282.

Quevedo, F.P.M., Bernaud, D., S., M., 2022b. Numerical integration scheme for coupled elastoplastic–viscoplastic constitutive law for tunnels. International Journal of Geomechanics 22. doi:10.1061/(ASCE)GM.1943-5622.0002512.